Tagging cosmic ray background at the Icarus detector

Alessandro Ruggeri

Under the supervision of:
Minerba Betancourt, PhD.

October 7, 2022

Abstract

ICARUS T-600 will be the Far Detector of the upcoming SBN program, for which it will leverage a $\sim$ 1ns response and a high resolution for neutrino event reconstruction. ICARUS will respond to the challenge of the cosmic flux at the surface thanks to its Cosmic Ray Tagging (CRT) system. The work conducted during the *Summer Students at Fermilab* program contributed to the calibration activities that are ongoing in view of the second physics run in late 2022: the timing of CRT and PMT signals was analysed, highlighting the need for corrections to the PMTs. The timing delay for the global trigger signal for a section of the side CRT. The possibility of calibrating the light yield of the side CRTs with run data was finally explored.

Contents

1 Searches for light sterile neutrinos

1.1 Theoretical aspects

Sterile neutrinos are hypothetical particles that do not interact by any of the known fundamental forces, except gravity. As such, the existence of sterile neutrinos must be inferred indirectly through their mixing with Standard Model neutrinos, which could drive new oscillation effects among the active flavours [1].

Originally introduced by Pontecorvo in 1967, sterile neutrinos are a fairly generic addition to the SM or to most of its extensions, featuring, in particular, in several proposed mechanisms for the generation of non-zero neutrino masses. The introduction of neutrino masses, made necessary by the unambiguous observation of oscillations, suggests the inclusion of a new Weyl fermions N^β to allow for a Yukawa term of the form:

$$\mathcal{L}_{\text{Yukawa}} \supset -y^{\alpha\beta}(i\sigma^2 H^*)L^\alpha N^\beta + h.c., \tag{1}$$

where H is the SM Higgs doublet, $L^\alpha = (\nu^\alpha, e^\alpha)^T$ are the SM lepton doublets while $\alpha = e, \mu, \tau$ and $\beta = 1 \ldots n$ are flavour indices. In general n can be different from three, with the only requirement being $n \geq 2$ so as accomodate the experimental evidence of at least two massive neutrino states. After the Higgs field acquires its expectation value v, the Yukawa lagrangian in Eq. (1) yields *Dirac* mass terms of the form:

$$\mathcal{L}_{\text{mass}} \supset -M_D^{\alpha\beta}\nu^\alpha N^\beta + h.c., \tag{2}$$

with $M_D^{\alpha\beta} \equiv y^{\alpha\beta}v/\sqrt{2}$. It is straightforward to verify that $(i\sigma^2 H^*)$ and L^α are $SU(2)_L$ doublets with opposite hypercharges of $+\frac{1}{2}$ and $-\frac{1}{2}$ respectively, corresponding thus to a total $SU(2)_L \times U(1)_Y$ singlet. It follows, therefore, that N^βs must be total singlets as well. The N^β fields are therefore called *sterile neutrinos*, because they couple neither to the strong and EM interactions nor to the weak interaction [2].

While sterile neutrinos are more broadly defined as neutral leptons with no ordinary weak interactions, the term is usually used to refer to the still hypothetical *right-handed* neutrinos. Indeed, if they exist, such neutrino fields would be weak isospin singlets with no weak interactions except through mixing with the left-handed neutrinos. Right-handed neutrinos could then produce a Dirac mass-term similar to the the one of charged fermions by coupling to ordinary neutrinos and a SM Higgs field according to Eq. (2). The smallness of the Yukawa coupling for a Dirac mass, of $\mathcal{O}(10^{-12})$, required by the current upper limits on neutrino masses [3] has led to theoretical models where neutrino mass terms involve higher dimensional operators. Sterile neutrinos feature in some of such models as well: in the *Type-I Seesaw Mechanism* the combination of Dirac and Majorana mass terms for left-handed

and right-handed neutrino fields leads to a scenario where, upon diagonalization of the mass matrix leads to active neutrinos with small masses $\sim m^2_{Dirac}/M_{heavy}$ and sterile neutrinos with masses $\sim M_{heavy}$, much heavier compared to all known particles. Nonetheless, many other model within the See-Saw framework, predict light sterile neutrinos as well [4].

1.2 Phenomenology of Light Sterile neutrinos

As of today, numerous neutrino experiments have established the existence of flavour oscillations between the three active neutrinos of the Standard Model. These oscillations are characterised by the so-called *solar* and *atmpspheric mass splittings*, respectively $\Delta m^2_{\odot} \simeq 7.4 \times 10^{-5}$ eV^2 and $|\Delta m^2_{atm}| \simeq 2.5 \times 10^{-3}$ eV^2, as well as by three mixing angles, $\theta_{12} = 34°$, $\theta_{13} = 8.6°$ and $\theta_{23} \sim 45°$. However, over the last decades, several oscillation experiments have obtained results that seem to indicate the existence of an additional neutrino flavour: these *short baseline* oscillation experiments point towards a fourth mass eigenstate of $\mathcal{O}$(eV). As then the LEP measurement of the invisible decay width of the Z boson constrains the number of light weakly interacting neutrinos to three, the additional neutrino flavour must be a sterile neutrino [2]. While the scenarios can include generic numbers n of light sterile neutrinos, the anomalies observed by short baseline experiments may be explained by a minimal $3+1$ model, where a single sterile neutrino is added to the spectrum. In such a case the $3+1$ mixing matrix becomes:

$$\begin{pmatrix} \nu_e \\ \nu_\mu \\ \nu_\tau \\ \nu_s \end{pmatrix} = \begin{pmatrix} U_{e1} & U_{e2} & U_{e3} & U_{e4} \\ U_{\mu 1} & U_{\mu 2} & U_{\mu 3} & U_{\mu 4} \\ U_{\tau 1} & U_{\tau 2} & U_{\tau 3} & U_{\tau 4} \\ U_{s1} & U_{s2} & U_{s3} & U_{s4} \end{pmatrix} \begin{pmatrix} \nu_1 \\ \nu_2 \\ \nu_3 \\ \nu_4 \end{pmatrix} \tag{3}$$

which can be parametrised in terms of matrices $R_{ij} = R(\theta_{ij}\delta_{ij}$ of rotation in the ij-plane by an angle θ_{ij} and a possible phase δ_{ij}:

$$U = R_{34}(\theta_{34})R_{24}(\theta_{24}, \delta_{24})R_{14}(\theta_{14}R_{23}(\theta_{23})R_{13}(\theta_{13}, \delta_{13})R_{12}(\theta_{12}, \delta_{12}) \tag{4}$$

As long as $\Delta m^2_{41} \gg |\Delta m^2_{31}|, \Delta m^2_{21}$ oscillations at Short Baseline experiments, with ratios between baseline L and neutrino energy E of $\mathcal{O}$(1 m/MeV) are well approximated by the two-flavour vacuum oscillation formula

$$P_{\alpha\beta} \simeq \delta_{\alpha\beta} - 4|U_{\alpha\beta}|^2(\delta_{\alpha\beta} - |U_{\alpha\beta}|^2)\sin^2\left(\frac{\Delta m^2_{41} L}{4E}\right), \tag{5}$$

so that active-to-sterile disappearance or active-to-active appearance oscillations with a frequency associated with the Δm^2_{41} mass splitting are direct evidences of sterile neutrinos [1, 4].

As most experiments are based on the production and detection of $\overset{(-)}{\nu}_\mu$ or $\overset{(-)}{\nu}_e$, the oscillation probabilities for the three main experimental channels,

$P_{\nu_e\to\nu_e}$, $P_{\nu_\mu\to\nu_\mu}$ and $P_{\nu_\mu\to\nu_e}$ are approximated at short baselines as [4]:

$$\begin{aligned} P_{\nu_e\to\nu_e} &\simeq 1 - 4(1-|U_{e4}|^2)|U_{e4}|^2 \sin^2(1.27\Delta^2_{41}L/E), \\ P_{\nu_\mu\to\nu_\mu} &\simeq 1 - 4(1-|U_{\mu4}|^2)|U_{\mu4}|^2 \sin^2(1.27\Delta^2_{41}L/E), \\ P_{\nu_\mu\to\nu_e} &\simeq 4|U_{e4}|^2|U_{\mu4}|^2 \sin^2(1.27\Delta m^2_{41}L/E), \end{aligned} \tag{6}$$

which can be re-written in terms of the mixing angles θ_{i4} as:

$$\begin{aligned} P_{\nu_e\to\nu_e} &\simeq 1 - \sin^2(2\theta_{14}) \sin^2(1.27\Delta m^2_{41}L/E), \\ P_{\nu_\mu\to\nu_\mu} &\simeq 1 - \sin^2(2\theta_{24}) \sin^2(1.27\Delta m^2_{41}L/E), \\ P_{\nu_\mu\to\nu_e} &\simeq \frac{1}{4} \sin^2(2\theta_{14}) \sin^2(2\theta_{24}) \sin^2(1.27\Delta m^2_{41}L/E). \end{aligned} \tag{7}$$

The oscillation channels presented above are the most immediately promising approach to to obtain evidence for sterile neutrinos, as the characteristic $\sin^2(\Delta m^2_{41}L/4E)$ dependence may allow to distinguish them from other possible explanations of experimental anomalies.

1.3 Experimental searches

The current status of eV-scale sterile neutrino oscillations is still undefined. While data supporting the mixing of light sterile neutrinos with the active species continues to be collected, several experiments studying channels that should be sensitive to such mixing have not observed anything beyond the three-neutrino mixing framework.

The experimental data relevant to short-baseline oscillations are most naturally categorised by the channels in Eq. (6,7) into three groups: ν_e-appearance, ν_e-disappearance and ν_μ-disappearance. The following will present the experimental results obtained in these three channels up to the present day.

1.3.1 The ν_e-appearance channel

The first experiment to observe the short-baseline neutrino anomaly was the Liquid Scintillator Neutrino Detector (LSND), which ran at the Los Alamos National Laboratories between 1993 and 1998. LSND used a decay-at-rest beam of $\bar{\nu}_\mu$ produced by impinging 800 MeV protons on a beam dump, with a $< 8\times10^{-4}$ contamination from $\bar{\nu}_e$. The $\bar{\nu}_e$ component of the beam was observed 30 m downstream of the beam dump in a 167 tons scintillator-doped mineral oil detector through the *Inverse β decay* signature. Events with ν energies between 20 and 52 MeV were used in the analysis, which resulted in the observation of $87.9 \pm 22.4 \pm 6.0$ $\bar{\nu}_e$ events above expectation, corresponding to a 3.8 σ deviation [5]. Given the ratio $L/E \simeq 0.8$ m/MeV of the experiment, the result could be interpreted in a neutrino oscillation formalism as due to an additional mass-splitting $\Delta m^2 \geq \mathcal{O}(0.1\ \text{eV}^2)$, thus implying an additional mass eigenstate compared to the three in the standard model.

To follow-up on the results of LSND, the SciBooNE/MiniBooNE was constructed at Fermilab, operating, since 2002 on neutrinos from the Booster Neutrino Beam, with an energy spectrum peaking at 700 MeV and a magnetic horn system that allows to select either ν_μ or $\bar{\nu}_\mu$. SciBooNE and MiniBooNE detectors acted respectively as the Near and Far detectors of the experiment, the former being a 10.6 ton scintillator-strip neutrino detector located at 100 m from the beam production point and the latter, at a baseline of 540 m, based on Cherenkov light detection in 800 tons of mineral oil. The two-detector configuration allowed to measure the unoscillated composition of the beam, thus improving the precision in the disappearance channel compared to what would be possible with MiniBooNE alone. The combination of higher energy and longer baseline makes MiniBooNE sensitive to the same range of L/E and thus to the same mass splitting of $\mathcal{O}(1\ \mathrm{eV}^2)$ as LSND. In the same ν_e-appearance channel as LSND, the MiniBooNE collaboration has observed an excess of electron-like events using both neutrino and antineutrino beams, leading to a 4.7 σ deviation from the expected background [6]. If interpreted as due to neutrino oscillations, the excesses are compatible with the LSND results, strengthening the short-baseline anomaly [1, 4].

1.3.2 The ν_e-disappearance channel

Other anomalies compatible with short-baseline neutrino oscillations have been reported over the years in the ν_e and $\bar{\nu}_e$ disappearance modes by experiments operating with neutrinos from nuclear reactors and intense radioactive sources.

The first result, referred to as the Reactor Anomaly, is a deficit in the number of $\bar{\nu}_e$ events in a number of experiments using fluxes from nuclear reactors at short baselines ($L/E \sim 1$ m/MeV). The deficit currently has a $\sim 3\ \sigma$ significance with respect to the theoretical expectations. Due to the difficulties in modelling the $\bar{\nu}_e$ flux in nuclear reactors, the anomaly was only highlighted after a re-evaluation, in 2011, of the neutrino spectra, and the size of the theoretical uncertainties involved in the models is still debated. More recent results from the Neutrino-4 experiment show evidence at 2.7 σ of oscillatory behaviour with best fit parameters $\Delta m^2_{N4} = 7.30\ \mathrm{eV}^2$, $sin^2\theta_{N4} = 0.36$ [7, 8].

A second ν_e-disappearance signal comes from the measured rate of neutrinos produced in intense radioactive sources in the PBq range. Such sources were used to conduct calibration runs for the Gallium-based solar neutrino detectors GALLEX and SAGE. The measured rate of events was found to have a deficit at the level of 3 σ compared to the predictions [1, 4].

1.3.3 The ν_μ-disappearance channel

While separate experiments operating in the previous two channels seem to point towards light sterile neutrino oscillations, the present situation for ν_μ-disappearance searches is quite different, as no deviation from the three-neutrino framework has been observed so far. The lack of such deviations is in tension with the $3+1$ oscillation model, in which the appearance and disappearance oscillation channels are coupled. The ν_μ-disappearance channel is best studied by experimental setups with both a near and a far detector, searching for a ν_μ deficit in the far detector compared to the initial composition of the beam. Apart from experiments of this type such as CCFR, CDHS, MINOS and SciBooNE/MiniBooNE, further constraints have come from the IceCube *neutrino observatory* search of a matter-driven resonance in the atmospheric $\overset{(-)}{\nu}_\mu$ spectrum [1, 4].

1.3.4 Conclusions

In summary, the current sterile neutrino oscillation status has several potential signals in the ν_e appearance and disappearance channels, but none for the ν_μ disappearance. In fact, the global analysis of the sterile neutrino hypothesis shows no overlap between the allowed regions for these two datasets, as illustrated in Fig.1. This corresponds to a 4.7 σ tension that does not depend strongly on constraints derived from any single experiment [1, 4].

2 The SBN program

The Short-Baseline Neutrino (SBN) program at Fermilab is designed to address the possible existence of light sterile neutrinos, put forward to explain the anomalous results that were detailed in Sec.1.3. SBN will test this important hypothesis question using multiple, functionally identical detectors along the same neutrino beam, which will ensure a world-leading sensitivity. The present section will illustrate the detectors and techniques used at SBN as well as the aims of the program for what concerns sterile neutrino oscillations.

2.1 The SBN detectors

The SBN program will feature three large *Liquid Argon Time Projection Chamber* (LArTPC) detectors placed along the existing Booster Neutrino Beam at Fermilab. These will be SBND (or Short-Baseline Near Detector), acting as near detector at 110 m from the production point, MicroBooNE, 470 m along the beam and ICARUS-T600, acting as the far detector at 600 m from the source. A scheme of the SBN detectors layout is shown in Fig.2.

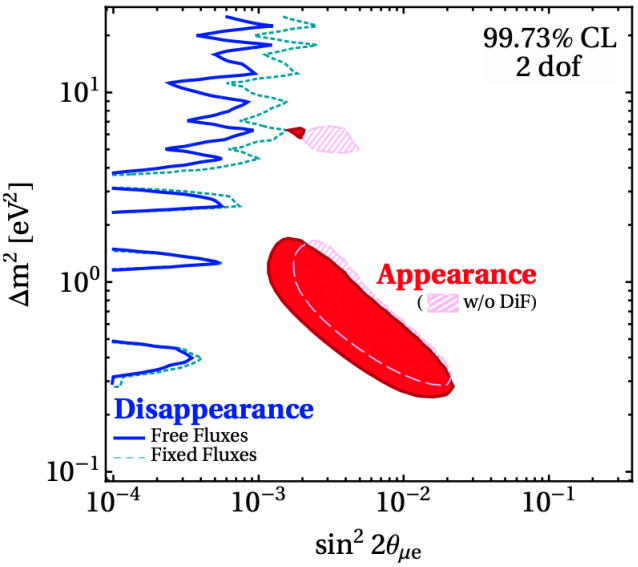

Fig. 1: Preferred regions in the $\sin^2\theta_{\mu e} \equiv 4|U_{e4}|^2|U_{\mu 4}|^2$ versus Δm^2 plane for disappearance dataset (using both free and fixed reactor fluxes) and for the appearance dataset, with and without the LSND decay-in-flight (DiF) sample. Curves are drawn at the 99.73% C.L. for 2 d.o.f. No overlap is present at the 3 σ level [1].

The use of multiple detectors measuring the same neutrino beam at different baselines will be key to the science goals of SBN. Furthermore, as the detectors will be functionally identical LArTPC, the systematic uncertainties when comparing event distributions at the different locations will be critically minimised. The neutrino sources used in the SBN program and the LArTPC detectors that make up the experiment are introduced in the following.

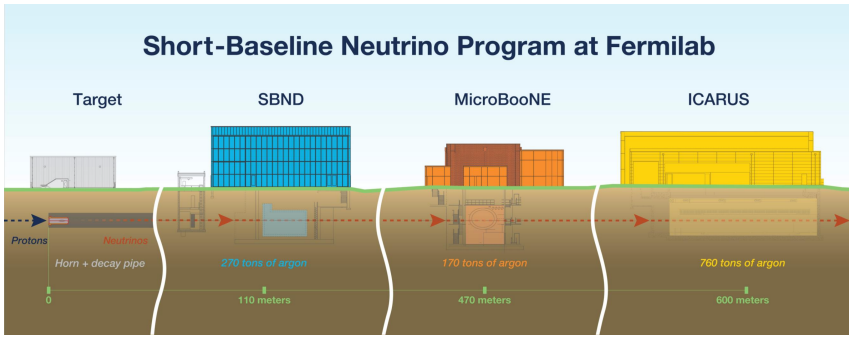

Fig. 2: Layout of the three SND detectors along the BNB neutrino beam.

2.1.1 Neutrino beams at FNAL

For its main experimental program, the SBN experiment makes use of the Booster Neutrino Beam (BNB) at Fermilab. The three detectors will be *on-axis* with respect to the beam direction. This neutrino beam is produced by impinging 8 GeV protons on a beryllium target to produce a beam of secondary hadrons, mostly pions. The charged secondaries are then focused by a single focusing horn magnet surrounding the target, in 143 μs pulses coincident with the proton delivery. The horn can switch the polarity of the pulses to select either positive or negative mesons. The majority of the focused mesons will decay to produce muon and electron neutrinos along the path through an air-filled decay tunnel.

The sign of the focused mesons determines the neutrino beam mode: mostly $\overset{(-)}{\nu}_\mu$ for positive (negative) mesons. BNB has already been operating successfully and stably for more than fifteen years in both neutrino and antineutrino modes, and its fluxes are well understood thanks to a simulation developed through data from the MiniBooNE and HARP experiments. The flux in neutrino mode is dominated by ν_μ (93.6%), followed by $\bar{\nu}_\mu$ (5.9%) from residual negative hadrons and with an intrinsic $\nu_e/\bar{\nu}_e$ contamination of $\sim 0.5\%$ at energies below 1.5 GeV. The BNB neutrino spectrum peaks at ~ 700 MeV.

For the MicroBooNE and Icarus-T600 detectors the higher energy NuMI neutrino beam will additionally be accessible, at an angle respectively 8° and 6° off-axis. This beam is produced by 120 GeV protons from the Fermilab Main Injector directed into a carbon target. The NuMI beam, in particular, will provide Icarus with a large sample of neutrino events in the 0-3 GeV range with an enriched ν_e component compared to the BNB spectrum ($\sim$ 5%) [1, 8].

2.1.2 The SBND detector

The Short Baseline Near Detector (SBND) is the planned near detector in the SBN program, with the aim of measuring the unoscillated BNB neutrino flux. SBND will be a 112 ton LArTPC placed 110 m downstream of the BNB target. It will have an active volume of 5.0 m (L) × 4.0 m (W) × 4.0 m (H) divided into two drift regions of 2 m, with a central cathode and two wire readout planes. The drift field, nominally of 500 V/cm, will be perpendicular to the neutrino beam, for a maximal drift length of 1.3 ms. Each drift volume readout is built from two coupled *Anode Plane Assemblies* (APA), consisting of 4.0 m × 2.5 m steel frames supporting three planes of wires spaced by 3 mm: two induction planes at ±60° from the vertical and a vertical induction plane.

SBND will feature a composite photon detection system, which will both enhance the amount of collected light and provide opportunities for R&D for

scintillation detection systems in LAr. The primary system consists of an array of 120 8" Hamamatsu photomultiplier tubes (PMTs) mounted behind the TPC wire planes, 96 of which are coated in TPB wavelength shifter. Together with the PMTs, the light detection system will feature novel 192 X-ARAPUCA photon traps modules instrumented with SiPMs.

Being located on the surface, SBND will necessitate a mitigation of the cosmic ray background in the detector. For this purpose the cryostat will be surrounded on all sides by a Cosmic Muon Tracker system based on scintillator strips with SiPM readouts. A 3 m thick concrete overburden will additionally be installed directly above the the detector.

SBND is currently scheduled to begin commissioning in 2023. The R&D effort for SBND will play a role in the development and testing of new technologies that will be featured in next generation neutrino experiments, most importantly DUNE [1].

2.1.3 The MicroBooNE detector

MicroBooNE is currently the world's longest running LArTPC, taking data from 2015 on. The detector consists of a TPC with an active volume of 87 tons, for a drift length of 2.5 m, a scintillation readout system based on 32 8" TPB-coated PMTs and a Cosmic Ray Tagger (CRT) system on the top and sides to reject cosmic ray events.

MicroBooNE has presently completed its physics run, producing the first high statistics precision studies of ν-Ar interactions both in inclusive and exclusive final states. It has additionally investigated the low-energy excess observed by MiniBooNE ($> 3\ \sigma$) of neutrino interactions producing final state electrons or photons. Both searches make up *Phase I* of the SBN program [8].

2.1.4 The Icarus T-600 detector

For the main physics program of SBN, the ICARUS T-600 detector will serve as far detector, located at 600 m from the BNB target. ICARUS, the first large-scale operating LArTPC detector, has already conducted a three-years run at the LNGS laboratories, imposing narrow constraints on the LSND signal by searching for a ν_e excess in the CNGS neutrino beam. After this first data-taking phase, the detector was moved to CERN where it underwent a significant overhaul between 2014 and 2016 in view of its future activity within SBN. The upgrades concerned the TPC readout electronics and light detection system, the construction of a new cold vessel and the refurbishment of the cryogenics. ICARUS was then transported to Fermilab in 2017, with the installation and filling with LAr being completed in 2020. Since then, the detector has completed the commissioning and started its first full-time run with neutrinos from BNB and NuMI in June 2021.

The ICARUS T-600 detector consists of two identical adjacent cryostat modules (T-300), each housing two LArTPCs made of three parallel wire planes, 3 mm apart, the first having horizontal wires and the other two at $\pm 60^{\circ}$ from the horizontal. The active volume in each of the T-300 modules are 18.0 m (L) $\times$ 3.2 m (H) $\times$ 3.0 m (W), for a total active volume of 470 tons. The two TPCs in each module are separated by a common central cathode. The maximal drift length is of 1.5 m, which corresponds to a drift time of about 1 ms for the nominal drift field of 500 V/cm. A new scintillation light detection system was installed during the overhaul phase: it consists of 360 TPB-coated PMTs, 90 in each TPC, providing a $\sim$ 1 ns time resolution and a sensitivity to energy deposits below 100 MeV.

As was the case for SBND, ICARUS will be placed just below the surface, and will thus be subject to a significant cosmic ray background. The main contribution to the background will come from cosmic muons traversing the detector and producing ν_μ and ν_e-like events. In addition, primary cosmic photons and neutrons can induce neutrino-like interactions in the detector. In order to mitigate these sources of background, a 3 m thick concrete overburden has been installed over the detector, with the purpose of removing the most part of photons and neutrons and suppressing the muon flux by $\sim$ 25%. Cosmic muons will therefore be the dominant background source inside ICARUS, and will thus be tagged in time and position by the *Cosmic Ray Tagging System* (CRT) that surrounds the detector. The calibration of the CRT of ICARUS was the main area of my activities at Fermilab, and as such, the system will be discussed in detail in the final section of this report [1, 8, 9].

2.2 Oscillation searches at SBN

The primary aim of the SBN program is to address the sterile neutrino interpretation of experimental anomalies that have been observed at short baselines over the past twenty years. SBN has several advantages over the previous experiments dedicated to light sterile neutrino ($\sim$ 1 eV) searches. Specifically the multi-detector design will be essential for achieving a world-leading sensitivity to short-baseline oscillations, while the locations of the near and far detectors are optimised for a maximal sensitivity in the most relevant ranges of oscillation parameters.

As illustrated in Fig.1, the global ν_e appearance data point towards a mass splitting Δm^2_{41} between 0.3 eV^2 and 1.5 eV^2 and a mixing angle in the range $0.002 \lesssim \sin^2 2\theta_{\mu e} \lesssim 0.015$. Oscillations will be visible at the ICARUS baseline (L = 600 m) for all oscillation parameters in the range indicated by global analyses, as Fig.3 shows. A strong sensitivity, in particular, is maintained at the far detector up to several eV^2.

For the main SBN physics run, an exposure of 6.6×10^{20} POT from BNB is planned, corresponding to three years of operation for both near and far

detector. In a 3+1 sterile neutrino scenario, such a data-taking period will be sufficient to reach. 5 σ sensitivities in almost all the currently allowed regions for both the ν_e-appearance and ν_μ-disappearance channels. Of particular importance will be SBN's capabilities to study ν_μ-disappearance channel, as its current tension with ν_e-appearance data is the primary challenge to the sterile neutrino interpretation. In Fig.4, the 3 σ and 5 σ sensitivities of SBN are shown, superimposed to several previous results for comparison.

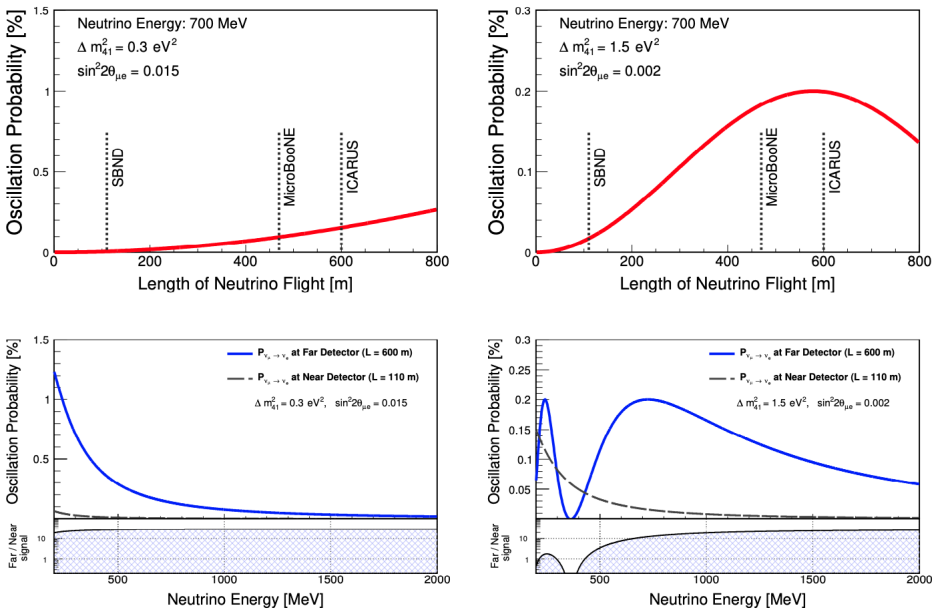

Fig. 3: *Upper panels*: oscillation probability in the $\nu_\mu \to \nu_e$ channel for 700 MeV neutrinos as a function of L for two benchmark point in the $3+1$ oscillation model. *Lower panels*: oscillation probabilities at the SBN near and far detectors as a function of the neutrino energy for the same benchmark points [1].

In addition to the main oscillation program, ICARUS will exploit both the BNB and NuMI beams to analyse the recent oscillation signal claim of the Neutrino-4 experiment, mentioned in Sec.1.3, as the two detectors have similar L/E ratios. A complete verification of the claim may be possible in less than one year, collecting $\sim$ 11500 ν_μ-CC events from BNB in three months and $\sim$ 5200 ν_e interactions from NuMI within one year [1, 8].

3 Calibration of the Icarus CRT system

The research project carried out during the internship period concerned the calibration and setup of the Cosmic Ray Tagging system (CRT) of ICARUS, in view of the second physics run starting in late 2022. Specifically, the two main lines of activity that were pursued were the implementation and verifi-

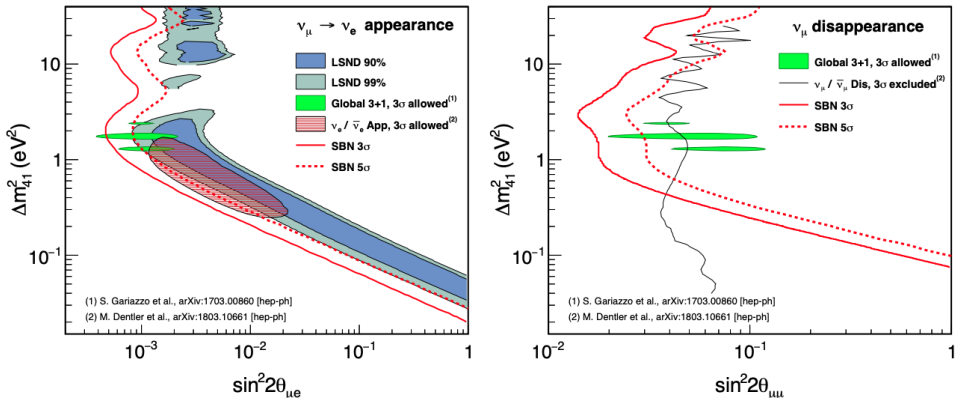

Fig. 4: SBN 3 σ (solid red line) and 5 σ (dotted red line) sensitivities to light sterile neutrino oscillations in the ν_e-appearance (*left*) and ν_μ-disappearance (*right* channels. Moreover, the LSND preferred regions for ν_e-appearance, the global ν_e-appearance and ν_μ-disappearance 3 σ regions as well as the 3 σ global best fit regions, are included for comparison in the corresponding plots [1].

cation of the timing corrections applied to the CRT signals and the calibration of the light-yield response of the side-CRT modules with respect to the hit position. After an introduction to the design and required performance of the CRT system of ICARUS, this section will discuss the research carried out during the Summer School period and the results that were obtained.

3.1 The ICARUS CRT system

3.1.1 Aims

As mentioned in Sec.2.1.4, during its run at SBN the ICARUS detector will be located at the surface, thus being exposed to a huge cosmic ray activity. Simulations of the cosmic background showed that cosmogenic interactions of all kinds depositing more than 100 MeV in the fiducial volume of ICARUS have a rate of $\sim$ 11 kHz, which for the *beam spill time* of BNB corresponds to an event every 50 beam spills. During its three-years physics run, corresponding to $\sim 1.32 \times 10^8$ spills at the nominal intensity, ICARUS will therefore detect 2.5×10^6 cosmic events during the beam spill time of the run, defined thus as *in-time cosmic activity*. Further *out-of-time activity* can occur during the drift time of beam-produced particles in each readout of the detector. The rate indicated above corresponds to $\sim$ 10 cosmogenic particles entering the detector volume during the 0.96 ms maximum drift time.

The in-time event rate of 0.83×10^6 cosmics per year, together with the $\sim$ 10 out-of-time tracks per readout, presents a significant experimental challenge in the search for sterile neutrino oscillations in the ν_e-appearance

channel, as a possible LSND-like signal in ICARUS would correspond to an excess of just $\mathcal{O}(100)$ ν_eCC events per year. Without cosmic ray mitigation systems, therefore, the detector would not be capable of carrying out any practical search.

The first cosmic background reduction strategy that has been implemented is the installation of a 3 m thick concrete overburden above the detector. The three layers of concrete blocks that form the overburden, equivalent to 6 m of water, allow to effectively remove all primary photons, reduce neutrons by a factor of 200 and suppress muons by 25%. Tab.1 lists the expected number of out-of-time particles crossing the active volume over a detector readout. Indeed, data collected after the installation was completed have shown a sensible reduction of the cosmic rate: from 600 (250) Hz to 330 (180) Hz for the horizontal (vertical) top CRT modules [10].

Particle	**Without OB**	**With OB**
$\mu^{\pm}$	15.5	11.5
p	< 0.045	$\ll 0.001$
γ	< 0.01	0
n	< 0.45	$\ll 0.01$

Tab. 1: Expected number of cosmogenic particles crossing the ICARUS active volume during the drift time with and without the overburden (OB) [10].

While the overburden is capable of absorbing more than 99% of the incoming photons and hadrons, it doesn't address the background from cosmic ray muons. In fact, from the event rate figures in Tab.2 follows that, at the nominal BNB intensity of 5×10^{12} pot/spill, only 1 νCC interaction every ~ 240 spills is expected to trigger the detector, compared to the rate of 1 every 55 spills from cosmic rays once the overburden is in place.

Event type	**Trigger rate**
ν_μCC in active volume	5.6×10^5
ν_eCC in active volume	3.5×10^3
νNC in active volume	2.1×10^5
Cosmogenic triggers	2.5×10^6

Tab. 2: Trigger rates in the active volume for the standard 6.6×10^{20} POT for ICARUS, delivered in 1.32×10^8 beam spills. The effect of the overburden is included: significant rate of crossing muons is retained.

The identification the subsequent rejection of cosmic ray muon tracks in the active volume will be possible thanks to the Cosmic Ray Tagging system surrounding the detector. This apparatus, consisting in several scintillator

detector modules with a $\sim 4\pi$ coverage, will provide the spatial ($\sim$ cm) and timing ($\sim$ 1 ns) coordinates of the track crossing point, thus allowing to tag cosmic charged particles with a 95% efficiency. Beam-induced muons produced by neutrino interactions outside the detector, known as *dirt muons*, will also be tagged by the CRT [10, 11].

3.1.2 Design

The CRT system of ICARUS consists of a Bottom, a Side and a Top CRT. Each subsystem is composed by plastic scintillator modules having two layers of scintillator, for a total CRT area of $\sim 1100\ \mathrm{m}^2$. The three CRT subsystems have different module designs:

- the Bottom CRT modules have been repurposed from the Double-CHOOZ experiment. They consist of two layers of 5 cm wide parallel scintillator strips, for a total of 32 strips. Readout is performed by a 64-pixel multi-anode PMT.
- the Side CRT modules have instead been repurposed from the MINOS experiment. Each module has 20 parallel scintillator strips in a double layer X-X configuration, with the exception of the upstream (south) wall, which has an X-Y configuration. The readout is performed by SiPMs.
- the Top CRT system is composed of 39 vertical modules along the sides and 84 horizontal modules covering the ICARUS top surface, capable of tagging alone 80% of incoming cosmic muons. Each module is an hodoscope composed of two orthogonal layers of eight23 cm wide scintillator bars. Each bar is readout on one end by a SiPM. Differently from the Side and Bottom CRTs, the Top CRT modules were anew for ICARUS at the Frascati National Laboratories.

Fig.5 shows the layout of the subsystems of the ICARUS CRT. As of September of 2022 all three subsystems have been installed, but the Bottom CRT modules are currently offline due to issues encountered by the electronics: work is ongoing to verify whether they can be put back to activity. Once online the Bottom CRT would prove valuable by measuring hits in coincidence with the Top CRT [10].

3.1.3 Cosmic ray tagging technique

For the tagging of cosmic ray events, ICARUS relies on the matching of CRT hits to the TPC tracks. The reconstruction of hits in the CRT modules is performed by exploiting the two-layer structure to determine the hit coordinates:

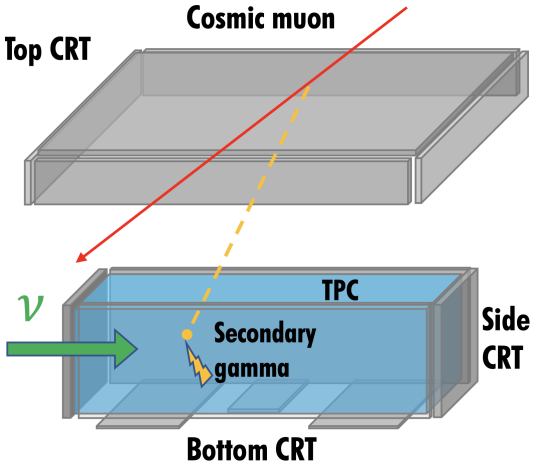

Fig. 5: Layout of the full ICARUS CRT system, showing the BNB beam direction (green arrow). Cosmic ray tracks in the active volume will produce scintillation emission and thus be triggered [10].

- for the Side CRT modules coincidences between the outer and inner planes of the modules are searched for within a 150 ns window. In the X-X configuration modules, the position along a strip is determined by the delay between the signals on the SiPM at either side of the module.
- in the Top CRT, hit reconstruction is performed by selecting the triggering channels in each layer and mapping them in detector coordinates.

According to the current algorithm, the TPC tracks are then matched to the reconstructed CRT hits that are closest to the projection of track on the CRT planes. In order for the matching to be valid, the position of the TPC tracks are corrected for their drift time. The algorithm is still being validated using a sample of cathode crossing tracks with known times [10].

Once CRT and TPC signals have been matched, it will be possible to discriminate cosmic ray events based on their Time of Flight:

$$ToF \equiv T_{CRT} - T_{PMT}, \tag{8}$$

where T_{CRT} is the time of the CRT hit matched to the event, while T_{PMT} is the time of the PMT flash inside the TPC. The rationale behind this criterion is that cosmic and dirt-muon tracks will enter the TPCs from outside and hit the CRT first, while the opposite is true for neutrino interactions, which will occur inside the TPC volume and produce outgoing tracks. Therefore, one expects $ToF > 0$ for neutrino events and $ToF < 0$ for cosmics. Indeed, preliminary Monte Carlo simulations of the ToF distributions feature such

a separation between the cosmogenic muon and BNB neutrino samples, as shown in Fig.6 [12].

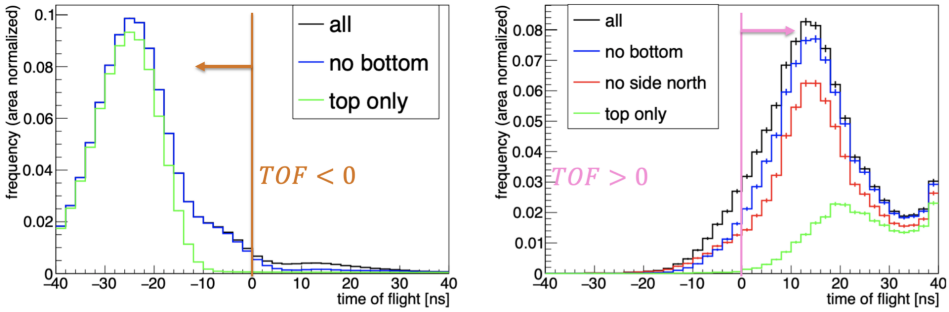

(a) Cosmogenic muons.

(b) BNB ν_μ.

Fig. 6: Preliminary simulations of the ToF distributions for a sample of cosmogenic muons (a) and one of BNB ν_μ events (b). The contributions of hits from different CRT subsystems are shown separately [13].

It becomes therefore clear that in order to discriminate the cosmic ray events, a precise determination of the time of the CRT and TPC signals must be achieved and all the subsystems of the ICARUS detector must be properly synchronised.

3.2 Timing corrections in the ICARUS CRT system

In order to reach a good rejection power in the discrimination of cosmic muons from neutrino events using the Time of Flight, a ∼ns precision level in the timing of the signals is necessary. As cosmics have fast ToFs, time offsets and jitters coming from the electronics of both the CRT modules and the PMTs must be verified and kept under control. The resulting corrections to the two systems must be then applied do the data when matching CRT hits and TPC flashes in order to have valid timing for the events.

Indeed, the first line of activity to be started during the internship was the validation of the timing of CRT hits and of the related corrections using ICARUS run data. This task made it possible to gain a better understanding of the features of the CRT system, the signals at play in timing and the potential sources of delay, as well as of the processing procedure involved in the CRT-PMT matching.

3.2.1 Timing of the CRT and PMT signals

Before discussing the results of the timing analysis in Sec.3.2.2, it is necessary to introduce the procedures used to determine the times of CRT hits and PMT flashes, from which the ToF is computed. The times of these two physical activities in the detector are retrieved from the saved raw timing

data through a chain of delays due to the physical propagation of signals and the workings of the trigger system.

In ICARUS the global trigger signal is generated by a majority of discriminated pairs of PMT signals being in coincidence with the neutrino beam spill gate interval. For every global trigger, CRT and TPC data for the 2 ms around the trigger time are recorded, allowing to tag cosmics crossings during the ~ 1 ms drift time. All times of an event are conventionally computed relative to the time T_{trig} of the global trigger signal ($T_{trig} = 0$), the latter corresponding to the measured value of the trigger time corrected for the cable delays along the signal path.

It is therefore clear that the PMT and CRT signals will be produced at earlier times than T_{trig}, as multiple delays will intervene between light detection by the PMTs and the production of a trigger. The PMT timings, in particular, will be given with respect to the digitised trigger logic start signal $T_{trig(digitised)}$, from which T_{trig} is recovered by correcting for the cable delay. As the PMT signal cable delays and the electron transit time in the tube are measured through the calibration lasers, it is thus possible to obtain the corrected PMT flash time T_{PMT} relative to T_{trig}. This is the time associated to the reconstructed light pulses.

The times of the CRT hits T_{CRT} are computed through the timing signals of the Front End Boards (FEBs) used in the modules. The FEBs (DT5702 model produced by CAEN) are instrumented with two independent counters $T0$ and $T1$:

- $T0$ defines the absolute, or global, time of the signals. It is reset with a pulse per second (PPS) signal provided by a White Rabbit network,
- the $T1$ counter is instead reset once a Global trigger signal is generated.

Therefore, at the time a global trigger is generated, the $T0$ corresponding to the reset of $T1$ counter ($T0_{trig}$) is recorded: this time is then corrected for the cable delays to recover T_{trig}. The CRT hit $T0$ is then calculated relative to T_{trig} to convert the absolute time into relative time. Further corrections for the cable delays and light propagation in the scintillator are then applied. Fig.7 presents a scheme of the timing for the Top CRT signal, specifying the delays introduced by the different stages of the distribution path.

Fig.8 shows instead a general scheme of the timing of the trigger, PMT and CRT, highlighting the distribution path of the signals and the consequent delay sources. The specific values of the delays vary between elements of the CRT and TPC, as these may be reached through different cable lengths. At the time of writing, delays introduced by some of the stages and components are still being measured and timing corrections are being implemented.

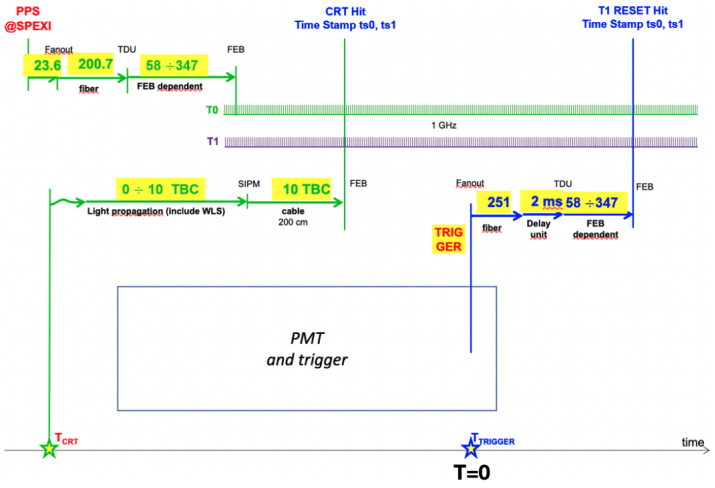

Fig. 7: Scheme of the timing of the Top CRT, showing the delays introduced by the distribution paths of the $T0$ counter, the global trigger signal as well as the CRT signal. These delays are corrected for in order to compute T_{CRT} (*courtesy of G. Sirri*).

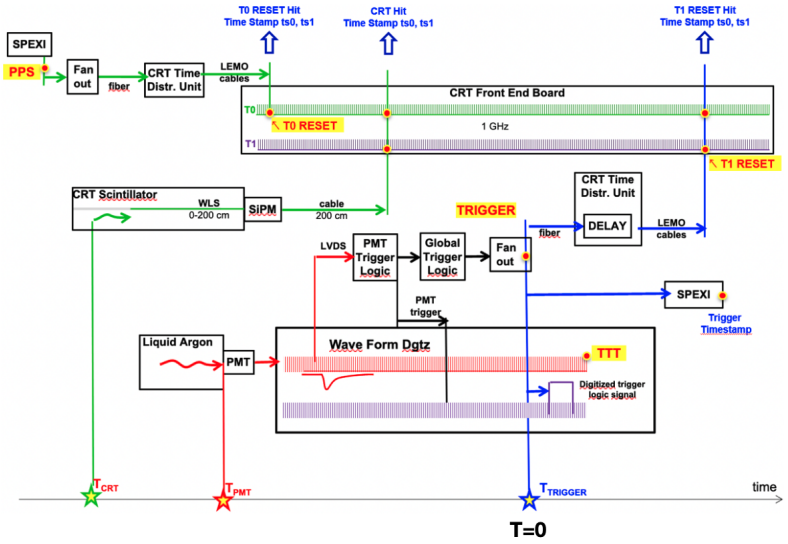

Fig. 8: General scheme of the timing of the PMT, CRT and trigger signals showing their distribution paths the consequent sources of delays. The correction of these delays allows to compute T_{PMT} and T_{CRT} and therefore obtain the ToF of the event (*courtesy of G. Sirri*).

3.2.2 Timing analysis

In the initial phase of the activity, the first timing analysis of NuMI beam events was conducted using the most recent timing corrections available at the time (August 2022). Specifically, a sample of 16419 NuMI events collected during the recent Run-8530 of ICARUS (July $3^{\text{rd}} - 5^{\text{th}}$ 2022) was used. The analysis of the raw data was conducted with local release of *Icaruscode v09_55_00* modified to include all the available timing corrections. As the original CRT-PMT matching module computed T_{CRT} with respect to the *timestamp* of the beam gate signal, a modification was included to calculate it relative to the timestamp of the global trigger $T_{trig\_tsp} = T0_{trig} - \langle \Delta_{FEB} \rangle$ produced by the SPEXI crate, where $\langle \Delta_{FEB} \rangle$ is the mean overall timing correction applied for a certain FEB of the CRT, of $\mathcal{O}(10$ ns). The T_{trig_tsp} reference was used as $T0_{trig}$ was not yet available in the analysis code version that was being used.

An initial check of the validity of the timing could be made by plotting the distribution of the CRT hit times T_{CRT} relative to the beam gate timestamps T_{gt_tsp}, which have T_{trig_tsp} as reference. The difference between the two times should show an excess of CRT hits from cosmic rays and dirt muons due to the trigger bias in time with the beam spill gate, which for NuMI is 9.5 μs wide. In Fig.9 the $T_{CRT} - T_{gt\_tsp}$ distributions for hits in the Side and Top CRTs are shown: the width of the excess has the expected value of 9.5 μs.

The most significant plot for the timing analysis was the distribution of the ToF for events with hits in the Side and Top CRTs. As $ToF = T_{CRT} - T_{PMT}$, corrections from both CRT system and the PMTs must be implemented for cosmic ray discrimination to be possible. The two plots, shown in Fig.10, presented two main issues:

1. the ToF values are not consistent with the order of magnitude expected from the modelling of the detector.

2. both plots show an extra peak, highlighted in Fig.10, to the left expected distributions.

The following paragraphs will discuss these issues in more detail.

Expected ToF values. The value of the ToF for an event is composed of several factors depending on the topology of the particle producing the signals on the CRT and on the PMTs. While the expectation value is not obvious, an estimate can be given considering vertical muon tracks that cross both the cathode and the CRT along the y direction. For such tracks the time of flight from the CRT to the LAr volume and the propagation time of the scintillation light are determined by the geometry, so that the mean

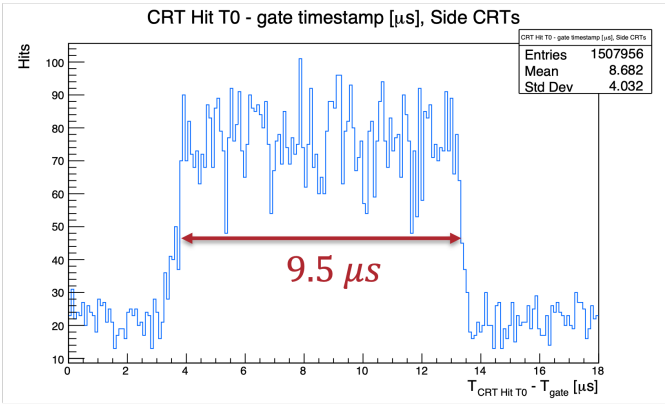

(a)

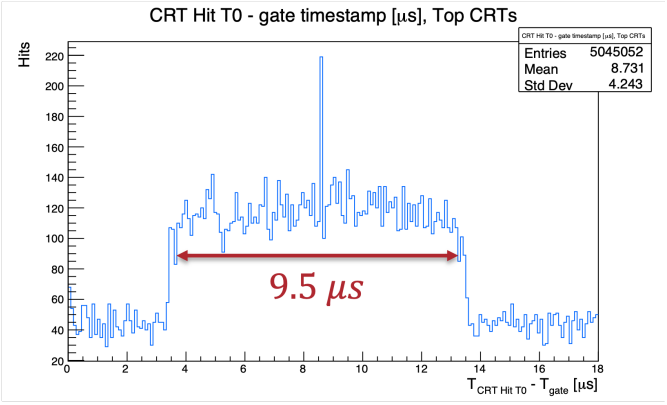

(b)

Fig. 9: Distributions of the CRT hit times T_{CRT} (here named Hit $T0$) relative to the NuMI beam gate start timestamp. Hits in the Side CRT modules are shown in (a), while the distribution for the Top CRT hits is in (b). Both distributions shows the 9.5 μs wide excess due to the trigger bias in time with the beam spill gate.

ToF can be estimated as:

$$\langle ToF \rangle = \Delta y_{\text{CRT-LAr}}/c + \Delta x_{\text{cath-PMT}} \cdot (1.38/c) \sim 30 \text{ ns}, \tag{9}$$

where $\Delta y_{\text{CRT-LAr}}$ is the vertical distance between the CRT and the LAr volume, and $\Delta x_{\text{cath-PMT}}$ is the distance between the central cathode and the PMTs. This shift by ~ 60 ns had been found to be produced by the use of T_{trig_tsp} as a reference for T_{CRT} instead of $T0_{trig}$. The issue would thus have to be addressed by the following versions of the CRT-PMT matching module in the Icaruscode software.

The extra ToF peak. The expectation for the Side and Top CRT ToF distributions would be to have respectively a double and a single peak struc-

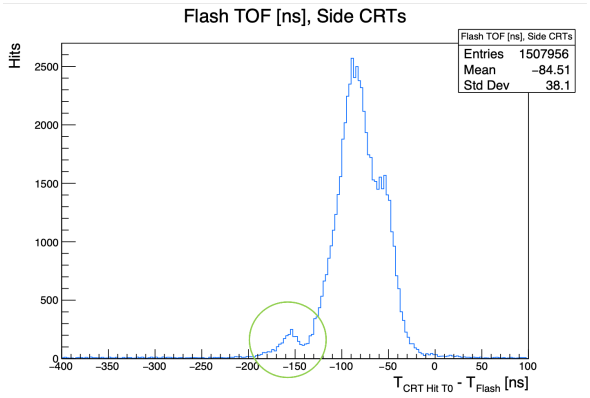

(a)

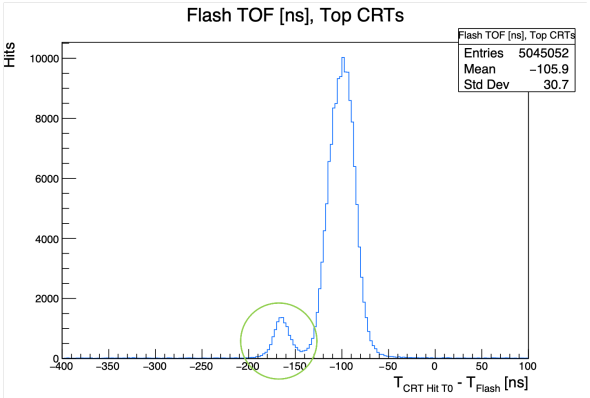

(b)

Fig. 10: Distributions of the ToF for events with hits in the Side and Top CRTs. The unexpected extra peaks are highlighted in green. $T0_{CRT} \equiv T_{CRT}$ is computed relative to T_{trig_tsp} as usual.

ture, due to the fact that:

- as the Side CRT has modules on opposite sides of the detector, it can act as both entry and exit point for cosmic muons. Entry hits will therefore occur before T_{PMT}, while exit hits will follow the passage through the TPC, leading to a double peak structure in the ToF plot.
- As the Top CRT is, for the most, part laid out on a single plane, it can only act as an entry point for cosmic ray particles, so that a single hit will occur per event. A single ToF peak is then expected.

As seen in Fig.10, the extra peak has the same position for both the Side and Top CRT distributions, which suggested an origin unrelated to the distribution of T_{CRT}. The ToFs were thus plotted separately based on the cryostat in which the flash was detected. As Fig.11 shows, the extra peak is present only in the distribution of events with flashes in the East cryostat.

The origin of the discrepancy could then be confirmed by plotting the distributions of the T_{PMT} flash times in the East and West cryostats, shown in Fig.12: the East cryostat distribution features an extra peak, compared to that of the West cryostat, which is instead consistent with previous timing analyses from BNB data. The extra peak was thus determined to be due to uncalibrated PMT channels in the East Cryostat.

After this first phase, the timing analysis activity slowed down while waiting for the release of updated corrections for the PMTs needed, among other things, to resolve the extra peak from the East Cryostat. The update, which contained several changes to the timing computation and corrections for the PMT system, could be merged on a local release of version v_09_58_01 of the Icaruscode software, itself containing up-to-date timing corrections for the CRT. In particular, the new Icaruscode version made it possible to implement the computation of T_{CRT} relative to $T0_{trig}$ in the CRT-PMT matching analysis module. As the PMT timing updates were released shortly before the end of the internship program, it was not possible to correctly merge them to the Icaruscode release. The correct procedure for the merging has since then been determined, yielding valid results on BNB data from Run-8552 [12].

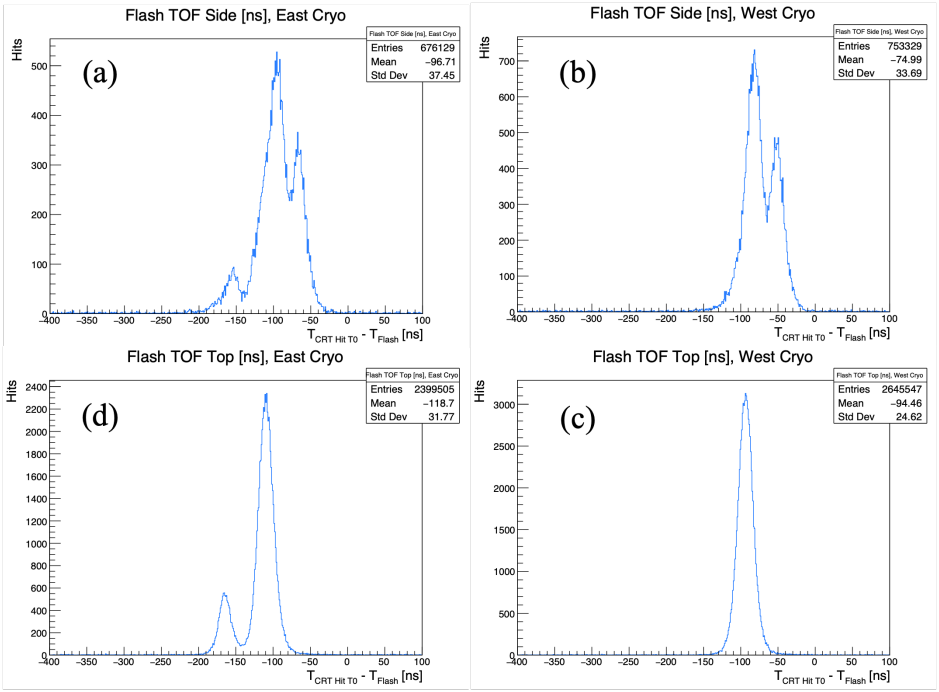

Fig. 11: *ToF* distributions for hits in the Side (**a** and **b**) and Top (**c** and **d**) CRTs, for PMT flashes in the two separate cryostats. The extra peak is only present in events with flashes in the East cryostat (plots **a** and **d**).

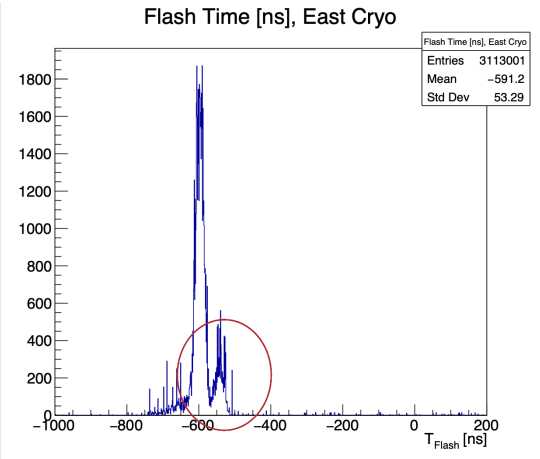

(a)

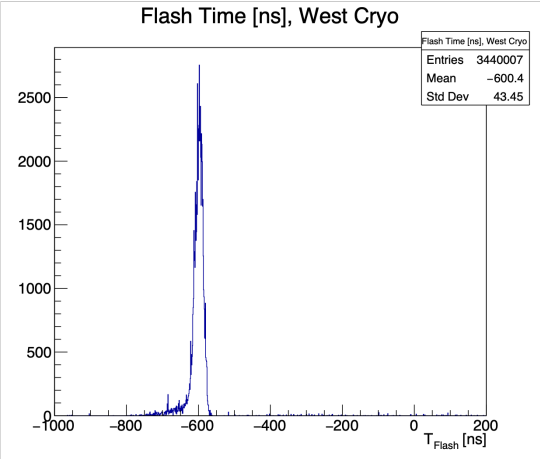

(b)

Fig. 12: Distributions of the T_{PMT} for flashes recorded in the East (a) and the West cryostat (b). The East cryostat distribution features an extra peak consistent with the one observed in the ToF plots.

3.2.3 Global trigger delay measurement

As clear from Fig.8, for the purpose of an accurate timing of the trigger, CRT and PMT signals, the delays occurring across the distribution paths must be measured and corrected for in the analysis. As a side activity to the analysis of the timing of CRT data, the measurement of the delay along the distribution path of the $T1$ reset signal through the Timing Distribution Unit (TDU) of the East and West Side CRTs was performed. The TDU distributes the $T1$ reset signals to the FEBs of the CRT, delaying it by 2 ms so as not to have dead-time in the readout during the drift time of the

beam spill window. A scheme of the $T1$ distribution path is shown in Fig.13: the time delay Δ_{T1} to be measured goes from the the Global Trigger Logic (GTL) output to the output of the TDU.

Despite having the same scheme, the distribution paths of the CRT sections will be subject to different delays as different cable lengths are required. In the present case, the East CRT TDU is located directly below the GTL crate, requiring a ~ 12.2 m long optical fibre. The West Side CRT TDU is instead located on the other side of the building form the GTL, for a ~ 36.6 m long fibre. The West CRT delay is thus expected to be larger than the East one by a substantial amount. The measurement was divided in two separate phases:

1. initially the delay Δ_1 between the CSU Fanout output and the TDU output was measured.

2. at a later time the delay Δ_2 between the GTL and the CSU outputs was then obtained and summed to Δ_1 to get the cumulative Δ_{T1} delay.

In both measurements, the delays were measured by an oscilloscope as those introduced by the distribution path between two synchronous square waves produced by a pulse generator. The 2 ms delay of the TDU was furthermore set to 0.

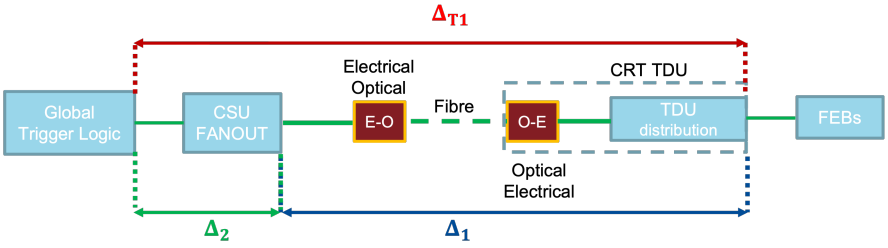

Fig. 13: Scheme of the distribution path of the $T1$ reset signal, showing the two measured delays Δ_1 and Δ_2.

Measurement of Δ_1. As the output of the CSU fanout is on a different floor from that of the CRT TDU, the measurement could not be performed by connecting the oscilloscope to both ends of the distribution path. The strategy outlined by the schemes in Fig.14 was instead used:

1. The connections in Fig.14a were first realised. In this way the oscilloscope would measure a delay $\Delta_{A+B} = \Delta_A + \Delta_B$ between the two square waves given by the sum of the two paths A and B. The connector cables from A to B had the same length so their generic T ns delay cancelled out.

2. The connections were then changed to those in Fig.14b. With this setup, the delay measured by the oscilloscope corresponded to the difference between the A and B paths, $\Delta_{A-B} = \Delta_A - \Delta_B$.

The needed delay $\Delta_1 = \Delta_A$ was then computed as:

$$\Delta_1 \equiv \Delta_A = [\Delta_{A+B} + \Delta_{A-B}]/2 = [\Delta_A + \Delta_B + \Delta_A - \Delta_B]/2. \qquad (10)$$

The oscilloscope allowed to make an histogram of the multiple measurements of the square-wave delays over several periods. The mean values of the gaussian histograms were taken as the value of the delays, with the measurement error given by the histogram's standard deviation. The procedure outlined above was conducted for the East and West CRT distribution paths.

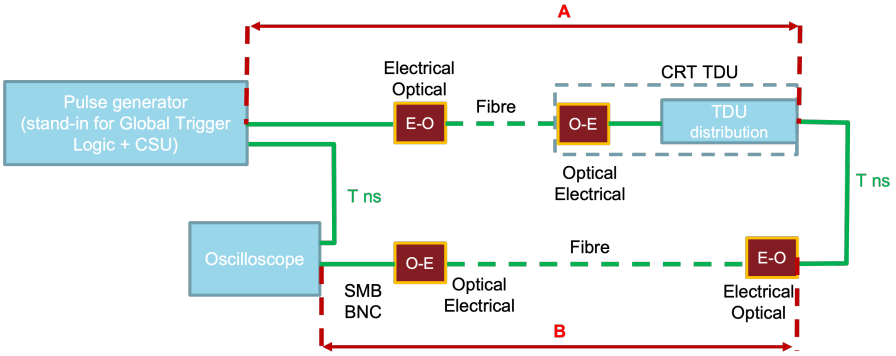

(a)

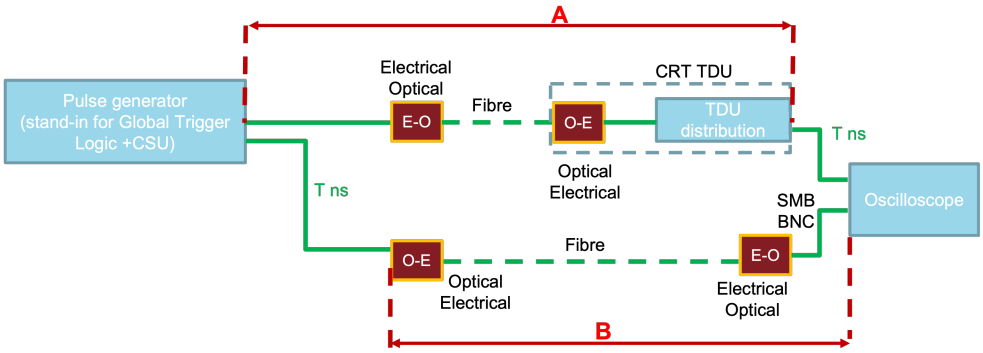

(b)

Fig. 14: Schemes of the two $A + B$ and $A - B$ connections used to measure Δ_1. The T ns cables have equal length, so that their generic delays cancel out.

Measurement of Δ_2. The measurement of the remaining delay in the distribution path of $T1$ was trivial to perform, as both ends of the path, from GTL output to the CSU output, are located in the same rack. As

shown in Fig.15 the oscilloscope was connected to both the Pulse generator and the CSU with cables of equal length. Connecting the GTL-to-CSU cable to pulse generator allowed thus to measure directly the delay from path A. The procedure was performed for the distribution paths of both East and West side CRTs.

The final delay times $\Delta_{T1} = \Delta_1 + \Delta_2$ are reported in Tab.3 for the East and West Side CRTs: as expected the West CRT delay is significantly higher than the East one.

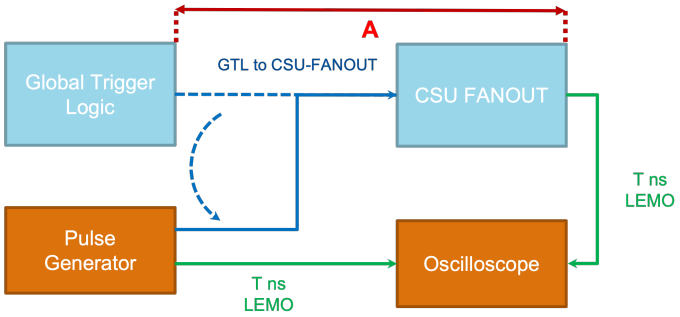

Fig. 15: Scheme connections realised to measure the Δ_2 time delay. The cable from the GTL to the CSU was connected to the Pulse Generator. Both LEMO cables to the oscilloscope had the same length, so that their delays cancelled out.

CRT side	$T1$ **signal delay**
East Side CRT	131.9 ± 0.2 ns
West Side CRT	251.4 ± 0.2 ns

Tab. 3: Measured delays Δ_{T1} of the $T1$ reset signal along the distribution paths for the East and West Side CRTs.

3.3 Calibration of the Side CRT light-yield

A second line of activity that was carried out during the internship was the calibration of the light yield of the Side CRT modules. As scintillation light traverses the CRT modules, a fraction of the photons will be absorbed by the plastic scintillator. In the Side CRT modules this results in a dependence of the light collected by the SiPM readouts on the coordinate along the scintillator bars. Modelling correctly such a behaviour would allow to obtain accurate Monte Carlo simulations of the light yield distributions inside the modules. This, in return, would open up the possibility of extracting calorimetric information from the side CRTs.

The latest study of the light yield behaviour with the position along a CRT strip was based on a test stand consisting of a MINOS CRT module, identical to the ones of the ICARUS Side CRT, and an hodoscope. This allowed to select normally incident cosmic ray events crossing the strips at a discrete set of distances from the only active readout. The behaviour of the light yield, given in terms of the number of photo-electrons (Pe) detected by the SiPMs, with the distance was thus obtained. The behaviour could be modelled by a quadratic decrease $Pe(z) = p_0 + p_1 \cdot z + p_2 \cdot z^2$, z being the distance from the active readout. The Monte Carlo total Pe distributions resulting from the fit parameters of the test stand, do not match exactly the data [14].

During the internship the possibility of performing a new calibration of the $Pe(z)$ response of the Side CRT modules using ICARUS run data was explored, the main difference from the test stand apparatus being that two readouts are active in the CRT modules. In order to extract fit parameters consistent with the test results, a dataset of cosmic ray events from Run-7923 of ICARUS was used, with the data analysis being carried out with Icaruscode v09_53_02. The following steps were performed:

1. the 2D histogram of the number of Pe versus the z coordinate relative to one of the readouts was obtained for layer 0 of one of the CRT modules, as shown in Fig.16a.

2. The profile of said histogram along the z axis, i.e. the average Pe for each bin in z, was then produced, as pictured in Fig.16b.

3. The central region of the profile was fitted by a sum of quadratic functions $P_1(z)$ and $P_2(z)$, corresponding to the responses of the readouts at both ends:
$$Pe_{tot}(z) = P_1(z) + P_2(8\text{ m} - z), \tag{11}$$
where $P_2(8\text{ m} - z)$ is the response of the readout opposite to the reference, as the CRT modules are 8 m wide.

4. The average of the quadratic parameters thus obtained were substituted to the test stand results as inputs of the Monte Carlo simulation of the light yield.

A Monte Carlo simulation of 500 BNB event was then produced using the new parameters as inputs for the calibration of the light response: the total Pe distribution that was obtained in this way has a much worse adherence to the true light yield distribution than the one resulting from the test-stand measurements.

The validity of the double fit procedure for calibration of the light yield has still to be established, and potential issues with the steps discussed above are being considered at the time of writing. Two main changes that could improve the results have been considered:

- The use of a dataset of CRT-PMT matched muon tracks with the constraint of the crossing of the cathode. Such tracks would have incidence angles on the CRT layers closer to the perpendicular, improving the consistency with the test stand data.

- The separation of the Pe contributions of the two readouts at both ends of the CRT modules. This would allow fit of the Pe vs. z response in much closer conditions to the ones of the test stand.

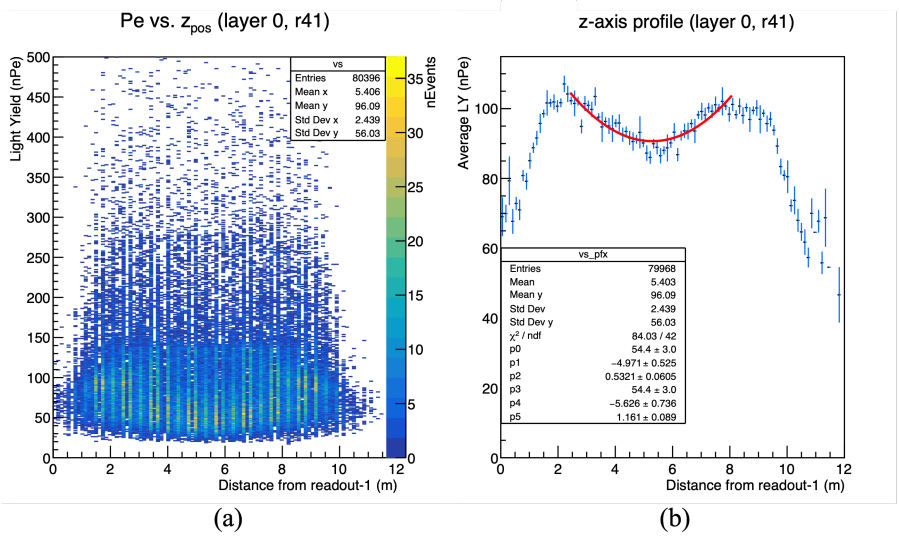

Fig. 16: In (**a**) the Pe vs. z histogram for layer 0 of one of the CRT modules (Center-West module) is shown. The profile of 2D histogram along the z axis is plotted in (**b**). The z coordinates are computed relative to the position of one of the end readouts of the module, indicated as *readout-1*. The parameters of the fit of to the $Pe_{tot}(z)$ function are shown in the statistics box.

4 Conclusions

The SBN program is set to perform a world-leading search for eV-scale sterile neutrinos with the aim of reaching 5 σ sensitivities in the currently allowed parameter regions. The ICARUS T-600 detector has the key role of Far Detector for the experiment: its installation at Fermilab has been successfully completed and its second full time neutrino run has started in June 2022.

The activities carried out during the internship concerned the calibration of the CRT. The timing of the CRT and PMT signals, which is crucial for the tagging of cosmic ray events, was analysed, finding the need for corrections

to be applied to the PMT channels. The delay along the distribution path of the $T1$ reset signal of the East and West Side CRT modules was measured. The possibility of light yield calibration of the side CRT using run data was finally explored: the calibration procedure was found to require further improvements.

The work on the timing and the calibration of the ICARUS CRT is currently being concluded, with the remaining timing corrections in the process of being accounted for in the event analysis, in time for the second physics run in late 2022.

5 References

[1] Pedro AN Machado, Ornella Palamara, and David W Schmitz. "The Short-Baseline Neutrino Program at Fermilab". In: *Ann. Rev. Nucl. Part. Sci.* 69 (2019), pp. 363–387. DOI: 10.1146/annurev-nucl-101917-020949. arXiv: 1903.04608 [hep-ex].

[2] Basudeb Dasgupta and Joachim Kopp. "Sterile Neutrinos". In: *Phys. Rept.* 928 (2021), pp. 1–63. DOI: 10.1016/j.physrep.2021.06.002. arXiv: 2106.05913 [hep-ph].

[3] K. A. Olive et al. "Review of Particle Physics". In: *Chin. Phys. C* 38 (2014), p. 090001. DOI: 10.1088/1674-1137/38/9/090001.

[4] J. M. Conrad and M. H. Shaevitz. "Sterile Neutrinos: An Introduction to Experiments". In: *Adv. Ser. Direct. High Energy Phys.* 28 (2018), pp. 391–442. DOI: 10.1142/9789813226098_0010. arXiv: 1609.07803 [hep-ex].

[5] A. Aguilar-Arevalo et al. "Evidence for neutrino oscillations from the observation of $\bar{\nu}_e$ appearance in a $\bar{\nu}_\mu$ beam". In: *Phys. Rev. D* 64 (2001), p. 112007. DOI: 10.1103/PhysRevD.64.112007. arXiv: hep-ex/0104049.

[6] A. A. Aguilar-Arevalo et al. "Significant Excess of ElectronLike Events in the MiniBooNE Short-Baseline Neutrino Experiment". In: *Phys. Rev. Lett.* 121.22 (2018), p. 221801. DOI: 10.1103/PhysRevLett.121.221801. arXiv: 1805.12028 [hep-ex].

[7] A. P. Serebrov et al. "Search for sterile neutrinos with the Neutrino-4 experiment and measurement results". In: *Phys. Rev. D* 104.3 (2021), p. 032003. DOI: 10.1103/PhysRevD.104.032003. arXiv: 2005.05301 [hep-ex].

[8] Maurizio Bonesini. "The Short Baseline Neutrino Program at Fermilab". In: *PoS* NuFact2021 (2022), p. 009. DOI: 10.22323/1.402.0009. arXiv: 2203.05814 [hep-ex].

[9] Christian Farnese and the ICARUS Collaboration. "Short-Baseline neutrino oscillation searches with the ICARUS detector". In: *J. Phys.: Conf. Ser.* 2156 (2021), p. 012141.

[10] F. Poppi on behalf of the ICARUS collaboration. *The Cosmic Ray Tagger system of the ICARUS detector at Fermilab*. Presented at the ICHEP 2022, 41° International Conference on High Energy Physics. Bologna, 8/07/2022.

[11] M. Antonello et al. "A Proposal for a Three Detector Short-Baseline Neutrino Oscillation Program in the Fermilab Booster Neutrino Beam". In: (Mar. 2015). arXiv: `1503.01520 [physics.ins-det]`.

[12] A. Heggestuen. *Event timing with the Cosmic Ray Tagger (CRT) and Photomultiplier Tube (PMT) systems*. Presented at the Icarus Collaboration Meeting. Frascati, 5/10/2022.

[13] Christopher Michael Hilgenberg. "Cosmogenic background rejection for the sterile neutrino search with the Short-Baseline Neutrino Program far detector". PhD thesis. Colorado State U., Colorado State U., 2020.

[14] J. Kim. *Light Yield Calibration*. Presented at the SBN FD CRT Working Group Meeting. 1/06/2022.